



**Design of multi-functional gel polymer electrolyte with 3D compact stacked polymer micro-sphere matrix for high-performance lithium metal batteries**

Journal:	<i>Journal of Materials Chemistry A</i>
Manuscript ID	TA-ART-03-2022-002085.R1
Article Type:	Paper
Date Submitted by the Author:	21-Apr-2022
Complete List of Authors:	Sun, Xiao-Guang; Oak Ridge National Laboratory, Chemical Science Division Liang, Jiyuan; Nanjing University, School of Chemistry and Chemical Engineering; Jiangnan University, Tao, Runming; Oak Ridge National Laboratory, Chemical Science Division Tu, Ji; Jiangnan University, Guo, Chi; Jiangnan University, Du, Kang; Jiangnan University, Guo, Rui; Jiangnan University, Wang, Zhang; Jiangnan University, Liu, Xiaolang; Jiangnan University, Wang, Deyu; Jiangnan University School of Chemical and Environmental Engineering, ; Tianmuhu Institute of Advanced Energy-Storage Technologies, Dai, Sheng; Oak Ridge National Laboratory,

# **Design of multi-functional gel polymer electrolyte with 3D compact stacked polymer micro-sphere matrix for high-performance lithium metal batteries**

Jiyuan Liang<sup>a\*†</sup>, Runming Tao<sup>bc†</sup>, Ji Tu<sup>a†</sup>, Chi Guo<sup>a</sup>, Kang Du<sup>a</sup>, Rui Guo<sup>a</sup>, Wang Zhang<sup>a</sup>, Xiaolang Liu<sup>a</sup>, Pingmei Guo<sup>a</sup>, Deyu Wang<sup>a</sup>, Sheng Dai<sup>bc\*</sup>, Xiao-Guang Sun<sup>c\*</sup>

a. Key Laboratory of Optoelectronic Chemical Materials and Devices of Ministry of Education, School of Optoelectronic Materials & Technology, Jiangnan University, Wuhan 430056, China

b. Department of Chemistry, University of Tennessee, Knoxville, TN 37996

c. Chemical Sciences Division, Oak Ridge National Laboratory, Oak Ridge, TN 37831, USA

† These authors contributed equally to this work.

## **Corresponding authors:**

E-mail: liangjy2004@126.com (Dr. J. Liang);

[dais@ornl.gov](mailto:dais@ornl.gov) (Dr. S. Dai)

[sunx@ornl.gov](mailto:sunx@ornl.gov) (Dr. X-G. S).

**Abstract:** Lithium metal batteries (LMBs) are considered as promising high energy density batteries. However, they are still suffering from poor cyclability due to the instability of solid electrolyte interphases (SEIs) and Li dendrite issues. Herein, a novel 3D dense-packed multifunctional crosslinked gel polymer electrolyte (PHGPE) has been synthesized by in-situ copolymerization of pentaerythritol tetraacrylate and 2-hydroxyethyl acrylate in a liquid electrolyte *via* a thermal initiation method. Due to intermolecular hydrogen bonding in the frameworks, PHGPE exhibits a 3D compact-stacking and crosslinked micro-sphere structure, which benefits the construction of homogenous  $\text{Li}^+$  flux, enabling uniform Li plating/stripping and formation of robust SEIs onto lithium electrode. Benefiting from the above advantages, symmetric Li cells in PHGPE deliver excellent cyclabilities of 6000 h at a current density of  $1 \text{ mA cm}^{-2}$  ( $1 \text{ mAh cm}^{-2}$ ) and 7700 h at  $0.5 \text{ mA cm}^{-2}$  ( $2 \text{ mAh cm}^{-2}$ ). Moreover, PHGPE has such a wide electrochemical window that it is compatible with both high-voltage  $\text{LiNi}_{0.8}\text{Co}_{0.1}\text{Mn}_{0.1}\text{O}_2$  and sulfur cathodes to realize long cycle life. Additionally, a  $\text{LiFePO}_4$  based pouch size LMB also presents promising performance. Therefore, this study of PHGPE has paved a new avenue for high-performance LMBs with excellent versatility and practicality.

**Keywords:** Gel polymer electrolyte; in-situ curing; lithium metal battery; solid electrolyte interphase (SEI); lithium dendrite

## 1. Introduction

In recent years, rechargeable lithium-ion batteries (LIBs) have been intensively studied and ubiquitously applied in various portable digital devices and large electronic vehicles due to their high energy density and energy conversion efficiency.<sup>1-6</sup> However, the traditional anode materials such as graphite (372 mAh g<sup>-1</sup>) and spinel lithium titanate (175 mAh g<sup>-1</sup>) have already reached their theoretical capacity limits and thereby failed to fulfill the ever-increasing demand of high energy density batteries. Alternatively, lithium metal (LM) has been considered as one of the most promising anode candidates for the next-generation high energy density lithium metal batteries (LMBs), due to its ultrahigh theoretical specific capacity (3860 mAh g<sup>-1</sup>), light weight density of 0.534 g cm<sup>-3</sup>, and the lowest electrochemical redox potential of -3.04 vs. the standard hydrogen electrode.<sup>7-9</sup>

Nevertheless, owing to the high reactivity of LMs, traditional carbonate based liquid electrolytes (LEs) with tremendous side reactions are unsuitable for the high-performance LMBs. Particularly, there are still a few obstacles that hamper the practical application of LM anodes: 1) the host-less nature of LM leads to infinite volume expansion, 2) the heterogeneous Li ion (Li<sup>+</sup>) flux at the solid electrolyte interface (SEI) results in uneven Li deposition; 3) the uncontrollable dendritic Li growth during Li plating/stripping not only causes dead Li with low Coulombic efficiency (CE) but also triggers safety concerns from potential shorting and thermal runaway. Therefore, developing highly stable LM anode is essential to realize the future large-scale energy storage and resolve the current energy crises. So far, various approaches such as using electrolyte additives to form stable SEI layer,<sup>10-12</sup> adopting solid-state electrolyte (SSE) to prevent Li dendrite from piercing the separator,<sup>13</sup> and building an artificial SEI layer to mitigate side reactions between LM and electrolyte,<sup>11, 14</sup> have been utilized to stabilize the LM anode and extend the cycle life of LMBs.

Compared to the commercial LEs that suffer from inhomogeneous Li deposition, unstable SEIs, low CE, and poor cyclability, SSEs possess excellent mechanical properties to suppress the formation of dendritic Li and effectively improve the long

cycling performance of LMBs. SSEs are generally divided into two types: inorganic ceramic solid electrolytes and solid polymer electrolytes. Although the inorganic ceramic electrolytes exhibit high ionic conductivity, they exhibit poor interphasial contact with the electrodes due to their stiffness, causing high interphasial impedance and high polarization and thereby limiting their electrochemical performance.<sup>15-17</sup> Additionally, the preparations of crack-free inorganic ceramic solid electrolytes are complicated, inevitably inducing high cost. Compared with the inorganic ceramic electrolytes, solid polymer electrolytes are more versatile and can be facilely prepared *via* in-situ or ex-situ polymerization methods directly on the surface of the electrodes.<sup>14, 18</sup> Unfortunately, solid polymer electrolytes usually have lower ionic conductivities than those of LEs and inorganic ceramic electrolyte at room temperature.<sup>19-23</sup> To enhance the ionic conductivities of solid polymer electrolytes, liquid electrolytes are usually introduced to obtain gel polymer electrolytes (GPEs).<sup>24-26</sup> However, in the case of single ion conductors, only organic liquids are needed to form GPEs, as lithium salts have already been fixed onto the polymer chains.<sup>27-30</sup> Unlike pure solid polymer electrolytes in which the polymer hosts must not only provide solvation groups such as ethylene oxide (EO) segments in polyethylene oxide (PEO) and propylene oxide (PO) in poly(propylene oxide) (PPO) etc. to dissociate lithium salts but also offer low glass transition temperature to facilitate ion migration within the polymer matrix to exhibit high ionic conductivities, GPEs are more flexible in selecting the polymer matrixes, as the ionic conductivity is mainly dominated by the liquid electrolyte in the GPEs.<sup>24</sup> Therefore, other polymers hosts such as poly(acrylonitrile) (PAN), poly(methyl methacrylate) (PMMA), polyvinylidene fluoride (PVdF) and Poly(vinylidene fluoride-*co*-hexafluoropropylene) (PVdF-*co*-HFP) with higher glass transition temperatures have also been intensively investigated in GPEs.<sup>24</sup> The gelation is formed by the hydrogen bonding interactions between the polar groups such as O (PEO, PPO, PMMA), N (PAN), and F (PVdF and PVdF-*co*-HFP) in the polymer matrixes and the abundant hydrogens both in the liquid electrolytes and the polymer matrixes. Not surprisingly, GPEs not only exhibit high ionic conductivities

that are comparable to those of LEs but also show excellent interphasial wettability like solid polymer electrolytes towards the electrodes.

One key parameter to prevent lithium dendrite formation is to maintain homogeneous current distribution during the lithium deposition process. Compared with the efforts of designing porous substrates as hosts for lithium to mitigate lithium dendrite growth,<sup>31-33</sup> it is much easier to design suitable GPEs to accomplish the same goal. First, unlike LEs that depend on the preformed porosities in commercial separators, homogeneous GPEs can be prepared by casting a homogeneous solution of liquid electrolytes and polymers. Second, GPEs can be prepared by facile polymerization of homogeneous solutions of liquid electrolyte and suitable monomers, with or without crosslinkers. Third, compact stacked GPEs with uniformly distributed pores can be designed by selecting suitable crosslinkers and co-monomers with desired functional groups, as well as tuning the ratio of the two precursors, which can enable homogeneous distribution of LE in the GPEs and current distribution, facilitating the growth of uniform SEI films on LM anodes and effectively inhibiting the formation of Li dendrites and ensuring long-life cyclability. Overall, the micro/nano structure of the polymer frameworks play a critical role in regulating the Li<sup>+</sup> flux. However, to the best of our knowledge, few works have been devoted to study the effect of micro/nano structure of polymer matrix on the behavior lithium deposition/dissolution.

Herein, we rationally design a multi-functional GPE with 3D crosslinked networks to regular Li deposition, which are assembled by sphere-like polymer particles (denoted as PHGPE) *via* a simple in-situ copolymerization and gelation of pentaerythritol tetraacrylate (PETEA) and 2-hydroxyethyl acrylate (HEA) in different LEs, as illustrated in Fig. 1a. As shown in Fig. 1b, in sharp contrast to the random stacked polymer matrix in GPEs formed by the self-polymerization of PETEA (PGPE), the stronger hydrogen bonding between the hydroxyl groups on the end chains of PHGPE constructs a 3D polymer micro-sphere network structure, providing a compact stacking gel polymer matrix with uniform channels for Li<sup>+</sup> migration, forming homogeneous Li<sup>+</sup> flux on the LM anode surface and promoting uniform Li plating. In addition, the in-situ polymerization process cannot only simplify the cell assembly process but also

enable constructing better electrode-electrolyte interphases, reducing interphasial impedance and ensuring long cycling stability. With these advantages, a symmetric Li cell in PHGPE achieves 6000 h cycling at a current density of  $1 \text{ mA cm}^{-2}$  with low overpotentials. Meanwhile, the abundant polar oxygen-containing groups in PHGPE not only broaden the electrochemical window of the electrolyte (up to 5.05 V) to allow its application for high voltage cathode materials, but also exhibit strong interactions towards lithium polysulfides (LiPSs) in Li-S batteries, mitigating the “shuttle effect” of LiPSs. Therefore, the in-situ polymerized PHGPE with 3D compact stacked micro-sphere matrix opens a new avenue for developing high-performance LMBs.

## 2. Results and discussion

As shown in Fig. 2a, the mixture of PETEA and HEA is a transparent liquid at room temperature. After thermal treatment at  $70 \text{ }^{\circ}\text{C}$  for 30 min, the polymerized mixture is a white semi-solid, which can stay at the bottom of the bottle even after turning it over, confirming that the LE is already absorbed into the porous structure of the PHGPE matrix. To confirm the polymerization reaction of PHGPE, Fourier Transform infrared spectroscopy (FTIR) was applied to monitor the structural evolution. As shown in Fig. 2b, the -OH stretching vibration of HEA at around  $3500 \text{ cm}^{-1}$ , C=O stretching vibration of PETEA at  $1726 \text{ cm}^{-1}$  and C=C stretching vibration of PETEA and HEA at  $1625 \text{ cm}^{-1}$  can be clearly observed.<sup>34</sup> However, after copolymerization, the peak of C-H asymmetrical stretching of  $\text{CH}_2$  at  $2940 \text{ cm}^{-1}$  is still present in PHGPE and its peak intensity is much stronger than that of PGPE, suggesting the successful copolymerization between HEA and PETEA. In addition, the disappearance of C=C and appearance of OH in PHGPE further indicate that PETEA and HEA precursors are indeed cross-linked, which is consistent with the  $^1\text{H}$  NMR spectra (Fig. S1).

To observe the micro-structure of the polymer matrix, SEM and TEM were performed on the dry gels. As shown in Fig. S2a & S2b, the SEM images of the PGPE matrix, self-polymerized by PETEA, show loosely packed structure and a random distribution of aggregated particles. TEM images (Fig. S2c & S2d) of PGPE matrix further reveal that these particles display a stacked lamellar structure without relatively

uniform size, which is therefore not beneficial to construct a homogeneous micro-structure of the GPE matrix. Interestingly, after co-polymerization with HEA, the PHGPE matrix is composed of uniform micro-spheres with a diameter of around 700 nm (Fig. 2c & 2d). TEM result (Fig. 2e) demonstrates that the micro-spheres have a solid structure. If examined closely, as displayed in Fig. 2f, the upper layered micro-spheres are stacked on the top of the gaps in the lower layered micro-spheres, facilitating to form a compact stacking structure, which favors homogeneous LE distribution in the pore channels as well as enabling even current distribution during lithium deposition.

The thermal stability of the GPE matrices was characterized by thermogravimetric analysis (TGA) in a nitrogen atmosphere. As shown in Fig. 2g, the two polymers show similar thermal properties. The first stage of weight loss below 100 °C is caused by the removal of physically adsorbed moisture. The second stage, due to the thermal decomposition, occurs in the temperature range of 100-500 °C, with a final weight about 18%. If examined closely, the stronger hydrogen bonding in the PHGPE matrix contributes to about 5.1 °C higher thermal stability than the PGPE matrix (inset of Fig. 2g).

The electrochemical properties of the electrolytes were first evaluated by linear sweep voltammogram (LSV) of Li||electrolyte||stainless-steel (SS) cells in a voltage range of 2 - 5.5 V at a scan rate of 1 mV s<sup>-1</sup>. As presented in Fig. 2h, the electrochemical stability window of PHGPE is 4.92 V *vs.* Li/Li<sup>+</sup>, which is higher than those of PGPE (4.42 V) and LE (3.81 V). This is mainly attributed to the hydrogen bonding in PHGPE because of the hydroxyl groups of HEA, increasing the oxidation potential of the electrolyte and opening the versatility for pairing with various electrode materials.<sup>35</sup> Besides the electrochemical stability window, Li<sup>+</sup> transference number ( $t_{\text{Li}^+}$ ) is another important parameter for evaluating the GPEs. According to the Bruce-Vincent-Evans equation,<sup>36</sup> the calculated  $t_{\text{Li}^+}$  of PHGPE is 0.62 (Fig. 2i), which is higher than those of PGPE (0.56, Fig. S3a) and LE (0.42, Fig. S3b). Such an observation is attributed to the interactions of the polymer matrixes, particularly the hydroxy groups, with the anions in the electrolyte, which improves the diffusion of Li<sup>+</sup>.<sup>37</sup> Overall, the higher  $t_{\text{Li}^+}$  of

PHGPE is beneficial to the uniform and dendrite-free Li deposition. Moreover, as an important parameter for practical application, the ionic conductivities of the gels were also explored. As shown in Fig. S4, the PHGPE displays an ionic conductivity of  $4.89 \times 10^{-4} \text{ S cm}^{-1}$  at 25 °C, which is higher than that of PGPE ( $3.62 \times 10^{-4} \text{ S cm}^{-1}$ ). The improvement is directly related to the introduction of HEA in the matrix, which benefits the construction of 3D compact stacked polymer micro-sphere network structures that facilitate fast  $\text{Li}^+$  transportation.

The improved interphasial kinetics is reflected by the nucleation overpotential of Li deposition on the surface of Cu foil. As shown in Fig. 3a, at a current density of  $1 \text{ mA cm}^{-2}$ , the nucleation overpotential in PHGPE is 5.6 mV, which is lower than that in PGPE (7.3 mV), and significantly lower than that in LE (31.6 mV). This result suggests that PHGPE can effectively reduce the nucleation potential of  $\text{Li}^+$  on the Cu foil, mainly due to abundant functional groups of the matrix, particularly the hydroxyl groups, that interact with the Li ions and reduces the Li nucleation energy barrier, thereby benefitting the lithium deposition. Furthermore, the 3D compact stacked micro-sphere matrix can provide  $\text{Li}^+$  transport channels to promote homogeneous transport of  $\text{Li}^+$  during Li deposition.

High coulombic efficiency (CE) is key to achieve long cycling stability in LMBs.<sup>38, 39</sup> To evaluate the CEs of the electrolytes, Li||Cu half-cells were assembled and tested by galvanostatic charge/discharge at a current density of  $0.5 \text{ mA cm}^{-2}$  with a fixed areal capacity of  $1 \text{ mAh cm}^{-2}$ . As displayed in Fig. 3b, the half-cell in LE presents a low initial CE value of 90.82%, which gradually increases to above 95% after a few cycles. However, the considerable fluctuation and dramatically decay of the CE after 20 cycles and 47 cycles, respectively, reveal that the formed SEI film is unstable, which repeatedly ruptures and repairs during Li the plating/stripping processes, resulting in the growth of Li dendrites and the decrease of CE. In sharp contrast, benefiting from the improved interphasial kinetics, the CEs of the half-cells in GPEs are significantly improved, especially in PHGPE. The initial CEs are 95.33 and 94.75% in PHGPE and PGPE, respectively. Compared with the cell in PGPE that can only maintain a relatively stable CE of 95.60% over 100 cycles, the one in PHGPE exhibits a significantly

improved CE of 98.35% over 130 cycles. Fig. 3c shows the charge/discharge profiles of the Li||Cu half-cells in different electrolytes at 50 cycles. The voltage difference between Li deposition and stripping in PHGPE is 29.8 mV, which is much lower than those in PGPE (39.3 mV) and LE (81.5 mV), further confirming the beneficial effect of PHGPE towards LM anode.

To further evaluate the compatibility of PHGPE with LM, symmetric Li cells in different electrolytes were subjected to long-term plating/stripping tests at different current densities. As shown in Fig. 3d, at a current density of  $0.5 \text{ mA cm}^{-2}$  and an area capacity of  $1 \text{ mAh cm}^{-2}$ , the cell in PHGPE exhibits the smallest overpotential of 49 mV and a remarkable lifespan of 1100 h. As a comparison, the polarization in PGPE and LE continually increases with random fluctuations, indicating an unstable LM-electrolyte interface and serious dendritic Li growth issues. Fig. 3e shows that the cell in PHGPE can maintain a flat voltage plateau, while those in PGPE and LE exhibit uneven voltage profiles, probably due to the uneven LM surfaces with cracks and voids, causing uneven Li deposition and dendrite formation on the LM surface, as analyzed in the following sections. Also, as shown in Fig. 3d, the initial and final polarization curves in LE and PGPE are higher than that in PHGPE, suggesting the unfavorable buildup of dead Li and significant Li dendrites, leading to short lifespan of the cells.<sup>11</sup> More impressively, at a higher current density of  $1 \text{ mA cm}^{-2}$ , the cell in PHGPE can still deliver an excellent cycling stability over 6000 h with a stable low overpotential of 121 mV (Fig. 3f and 3g). In addition, Fig. S5a & 5b show that the cell in PHGPE can be cycled under a high current density of  $3 \text{ mA cm}^{-2}$  for 1180 h with a low overpotential of 150 mV, which is comparable to its initial overpotential of 140 mV. Furthermore, to challenge thick homogeneous polymer-induced Li deposition,<sup>7, 40</sup> a higher areal capacity of  $2 \text{ mAh cm}^{-2}$  was utilized. Fig. S3c-d shows that the cell in PHGPE can be stably cycled for over 7700 h under a current density of  $0.5 \text{ mA cm}^{-2}$ , exhibiting a low overpotential of 40 mV. Even at a high current density of  $1 \text{ mA cm}^{-2}$ , it still delivers a highly promising lifespan of 960 h with a gradual decline of overpotential from 170 mV to 142 mV (Fig. S5e-f). The initial gradual decrease of overpotential is caused by the high reactivity of LM towards the electrolyte, which gradually passivates the

electrode and improves the interface between LM and gel electrolyte. Meanwhile, the morphology of LM after long cycling was also characterized with SEM to gain a deeper insight into the Li plating behavior. As shown in Fig. S6a, after cycling for 960 h, the surface of LM is relatively smooth, and no severe Li dendrite is observed. In addition, the electrochemical impedance spectroscopy (EIS) of the symmetric Li cell was also monitored before and after cycling. The total cell impedance increases from 90  $\Omega$  before cycling to 120  $\Omega$  after 960 h cycling (Fig. S6b), indicating the stability of the electrode interface and superior Li stripping and deposition performances in PHGPE. The above results suggest that PHGPE can form stable SEI, suppress Li dendrites and benefit long cycling stability of LMBs, resulting from its unique 3D compact-stacked microsphere matrix and functional groups that promote uniform Li deposition. More importantly, to the best of our knowledge, the symmetric Li cell in PHGPE successfully achieve the best long cycling stability (Table S1), demonstrating the outstanding compatibility of PHGPE with LM.

To reveal the composition of SEIs, depth profiling X-ray photoelectron spectroscopy (XPS) was employed to analyze the above cycled LM anodes. As shown in Fig. 4a-c, the deconvoluted results of the C 1s high resolution X-ray photoelectron spectra (HRXPS) for the three SEI layers exhibit five similar peaks, which are C-C/C-H at 284.8 eV, C-O-C at 286.3 eV, LiCOO-R (R for alkyl groups) at 288.6 eV, Li<sub>2</sub>CO<sub>3</sub> at 290.1 eV and C-F at 292.9 eV, respectively.<sup>41</sup> The F 1s spectra (Fig. S7) shows two peaks at 684.5 eV for LiF and 688.7 eV for CF<sub>2</sub>.<sup>23</sup> Meanwhile, the Li 1s spectra (Fig. S8) show four peaks at 54.38 eV, 54.88 eV, 55.38 eV and 56.88 eV, corresponding to Li<sub>2</sub>O, LiCOOR, Li<sub>2</sub>CO<sub>3</sub> and LiF, respectively.<sup>1, 42</sup> It is noted that both LiF (Fig. S7) and Li<sub>2</sub>CO<sub>3</sub> (Fig. S8) increase with the etching depth. The HRXPS of O 1s (Fig. S9) are consistent with the Li 1s spectra (Fig. S8).<sup>43</sup> It is also noted in Fig. 4a and 4b that the intensity of the main component of SEI, the organolithium salt (LiCOOR), decreases much faster with the etching depth in PHGPE (Fig. 4c) than it does in LE and PGPE, suggesting that PHGPE tends to form a much thinner and compact SEI that benefit for long cycling stability,<sup>44</sup> which is consistent with the above cycling data and the SEM results. According to previous studies, SEI can be divided into two layers, the inner and

the outer ones.<sup>45, 46</sup> Inner SEI is composed of inorganic lithium salts such as LiF and Li<sub>2</sub>O, whereas the outer SEI is mainly derived from the electrolyte decomposition with main components being organic lithium salts.<sup>47</sup> These organic Li components are poor ionic conductors, which are not beneficial to Li<sup>+</sup> transport, leading to nonuniform Li deposition and thus unfavorable electrochemical performances.<sup>48</sup> Typically, the more side reaction occurs, the more organic lithium salts are formed and thicker SEI layers are generated. Based on the above analysis, it can be inferred that PHGPE tends to form a more even and thin SEI that benefit for kinetic processes. As shown in Fig. 4d-e, the surface of pristine LM is relative flat and smooth. However, after 20 cycles at a current density of 0.5 mA cm<sup>-2</sup> with an areal capacity of 1 mAh cm<sup>-2</sup>, long needle Li dendrite morphology with more cracks is observed in LE (Fig. 4f-g). The Li dendrite is more suppressed in PGPE (Fig. 4h-i), but it is still more rough with the presence of many cracks and aggregated dead Li. As a contrast, benefiting from the homogeneous Li<sup>+</sup> flux and stable SEI, the Li dendrite is totally suppressed in PHGPE, leading to a compact and flat dendrite-free LM surface (Fig. 4j-k).

To obtain an in-depth understanding of the origin of the electrolyte effect on Li deposition, COMSOL Multiphysics was applied to simulate the Li deposition behavior.<sup>25</sup> In LE, an inhomogeneous current density distribution is observed, with high Li<sup>+</sup> flux on the top of Li nucleus and Li<sup>+</sup> is preferentially deposited on these protruding “hot spots”, favoring the formation of Li dendrites on the LM surface (Fig. 4l). In PGPE, a severe polarization in the electrolyte and many “hot spots” around the Li nucleus can be formed, inducing Li<sup>+</sup> being deposited around the Li nucleus and eventually leading to the formation of particle-like Li dendrites. In contrast, a uniformly dispersed Li<sup>+</sup> flux without obvious “hot spots” is observed on the surface of Li nucleus in PHGPE, favoring uniform Li deposition.<sup>1, 42</sup> Such a contrast result is mainly due to the 3D compact stacked micro-sphere matrix of PHGPE, which not only facilitates homogeneous Li<sup>+</sup> flux distribution but also enables uniform Li plating, generating a smooth Li deposition layer and effectively suppressing Li dendrites.<sup>49</sup> These simulation results are consistent with the observed Li surface morphology. Therefore, it can be confirmed that the PHGPE 3D micro-sphere crosslinked network structure

simultaneously provides homogeneous  $\text{Li}^+$  migration channels for uniform Li deposition and leads to the formation of stable SEI, which suppress Li dendrites and support long cycling stability of the LM anode.

To demonstrate the practicality and versatility of PHGPE in LMBs, PHGPE was evaluated in various cathodes based LMBs. Fig. 5a shows the cycling performance of NCM811 (areal mass loading:  $17.1 \text{ mg cm}^{-2}$ ) based LMBs in different electrolytes at a current density of 0.2 C. Apparently, the LMB in PHGPE exhibits not only the highest capacities but also the best long cycling stability. Particularly, the initial specific capacity in PHGPE is  $177.4 \text{ mAh g}^{-1}$  or  $3.03 \text{ mAh cm}^{-2}$ , which is higher than those in PGPE ( $169.3 \text{ mAh g}^{-1}$  or  $2.89 \text{ mAh cm}^{-2}$ ) and LE ( $133.3 \text{ mAh g}^{-1}$  or  $2.28 \text{ mAh cm}^{-2}$ ). It is interesting to note that, only the cell in PHGPE can deliver a comparable performance like the commercial LIBs, which have a minimum areal capacity of  $3 \text{ mAh cm}^{-2}$ .<sup>8, 50</sup> After 150 cycles, the specific capacity in PHGPE still maintains at  $143.5 \text{ mAh g}^{-1}$  with a capacity retention of 80.9%. On the contrary, the capacity in PGPE is only  $121.2 \text{ mAh g}^{-1}$  after 141 cycles with a capacity retention of 71.6%. The LMB in LE exhibits a much lower capacity that lasts only 55 cycles, which is ascribed to the depletion of electrolyte cause by the uncontrollable Li dendrites growth and poor SEIs and low CEs. Correspondingly, as the charge/discharge profiles shown in Fig. 5b, the LMB in PHGPE exhibits the smallest voltage hysteresis among the three electrolytes, probably resulting from its improved interfacial stability with LM anode and low total cell impedance (Fig. 3).

Lithium-sulfur (Li-S) batteries have attracted world-wide attention as the next-generation energy storage system, due to sulfur's high theoretical specific capacity of  $1672 \text{ mAh g}^{-1}$  and energy density of  $2600 \text{ Wh kg}^{-1}$ . Unfortunately, the dissolution of lithium polysulfides (LiPSs) in the electrolyte and their "shuttle effect" have impeded the successful commercialization of Li-S batteries.<sup>51</sup> Considering the enriched polar oxygen-containing functional groups in the PHGPE matrix that could effectively interact and inhibit the "shuttle effect" of LiPSs, Li-S cells were assembled and evaluated. Fig. 5c shows that the Li-S cell in PHGPE exhibits high capacities of 1305.4, 1047.0, 813.3, 615.0, 433.0, and  $259.5 \text{ mAh g}^{-1}$  at current densities of 0.1, 0.2, 0.5, 1,

2, and 5 C, respectively. Impressively, when the current density recovers back to 0.1 C, the cell still successfully delivers a high reversible specific capacity of 1162.3 mAh g<sup>-1</sup>, demonstrating its promising cycling stability. In contrast, the rate performance in LE and PGPE is much worse than that in PHGPE, probably due to their serious “shuttle effect” of LiPSs. Fig. 5d compares the charge/discharge profiles of the Li-S cells in different electrolytes at a rate of 0.5 C. Notably, the voltage hysteresis in PHGPE is 0.147 V, which is much smaller than those in PGPE (0.162 V) and LE (0.227 V). The reduced polarization is attributed to the improved interphasial kinetics between the electrodes and PHGPE, facilitating the transport of Li<sup>+</sup>. Fig. 5e shows the long-term cycling stability of the Li-S cells at 0.5 C. There are obvious capacity decays in LE and PGPE within the first 100 and 40 cycles, respectively. After 600 cycles, the capacities in LE and PGPE are 112.9 mAh g<sup>-1</sup> and 435.6 mAh g<sup>-1</sup>, corresponding to an average capacity fading of 0.07% and 0.14% per cycle, respectively. Surprisingly, the cell in PHGPE exhibits an initial capacity of 873.9 mAh g<sup>-1</sup> and there is no significant capacity attenuation observed; after 600 cycles, it delivers a capacity of 557.2 mAh g<sup>-1</sup> with an excellent capacity retention of 64%, corresponding to a capacity fading rate of 0.06% per cycle.<sup>52</sup> The excellent cycling stability in PHGPE results from its synergistic effects on enabling stable cycling of the LM anode and suppressing the “shuttle effect” of polysulfides *via* both physical and chemical adsorptions due to its porous structure and the abundant polar carbonyl groups and hydroxyl groups,<sup>53, 54</sup> which is well illustrated in Fig. 5f.

To investigate the practicality of PHGPE, LMBs with LiFePO<sub>4</sub> as the cathode were further assembled and evaluated. Fig. 6a shows the rate performances of the LMBs in the three electrolytes at different current rates. Obviously, the LMB in PHGPE delivers the best rate performance. For example, a high capacity of 148.7 mAh g<sup>-1</sup> is achieved at a high current rate of 2 C, which is 95% of the initial capacity at 0.1 C. In sharp contrast, the specific capacities in PGPE and LE at 2 C are only 110.8 and 79.4 mAh g<sup>-1</sup>, respectively. The galvanostatic charge/discharge curves in different electrolytes are also presented in Fig. 6b and Fig. S10, which further illustrate the advantage of PHGPE. Fig. 6c shows the cycling performance of the LMBs in different electrolytes at a high

current rate of 2 C. After 250 cycles, the cells in PGPE and LE deliver low capacity retentions of 88.6% and 61.6%, respectively. Remarkably, the cell in PHGPE can still maintain a capacity of  $123.9 \text{ mAh g}^{-1}$ , which is equivalent to 98.4% of its initial capacity. The sensational long cycling performance in PHGPE is ascribed not only to its stability against Li anode *via* formation of a stable SEI that can induce a uniform Li deposition and suppress the growth of Li dendrites but also to its overall low cell impedance.<sup>55-57</sup> As shown in Fig. 6d, the total cell impedance in PHGPE is  $82.4 \Omega$ , which is significantly lower than those in PGPE ( $114.3 \Omega$ ) and LE ( $164.4 \Omega$ ). To further demonstrate the practicability of PHGPE, one 1 Ah pouch cell was assembled (detailed parameters can be found in Fig. S11 and Table S2) and evaluated. As shown in Fig. 6e, the pouch cell can be cycled for 8 cycles without any obvious capacity decay, suggesting that PHGPE is very promising for application in large-scale LMBs. Fig. 6f shows that the pouch cell can fully power the light-emitting diode (LED) bulbs. More interestingly, as shown in the Video S1, the pouch cell can simultaneously power four small fans, further demonstrating the excellent practicality of PHGPE as a state-of-the-art GPE for electrochemical energy storage devices.

### 3. Conclusions

In summary, a novel gel polymer electrolyte with 3D crosslinked network structure has been successfully prepared by a facile in-situ polymerization of PETEA and HEA in the presence of LE. Benefiting from the 3D compact stacked polymer micro-sphere matrix and the formed stable SEI on the LM anode in PHGPE, uniform Li plating/stripping can be achieved, which has significantly improved the cycling stability of LM. High voltage cathode NCM811 based LMB in PHGPE achieves a high specific capacity of  $143.5 \text{ mAh g}^{-1}$  with a good capacity retention of 80.9% over 140 cycles. In addition, the abundant hydroxyl groups in PHGPE effectively adsorb LiPSs and suppresses the “shuttle effect” in Li-S batteries, delivering a reversible capacity of  $557.2 \text{ mAh g}^{-1}$  at 0.5 C over 600 cycles with an ultralow capacity degradation of 0.06% per cycle. Furthermore, the versatility and practicality of PHGPE is well-demonstrated

in LFP LMBs. The promising versatility and practicality of PHGPE in high-performance solid-state LMBs may also enlighten the studies of other energy storage systems such as sodium ion batteries, zinc ion batteries.

#### 4. Experimental section

*Materials:* Pentaerythritol tetraacrylate (PETEA, >97.0%) was purchased from Macklin Biochemical Company (shanghai). 2-hydroxyethyl acrylate (HEA, >96%) and 2, 2-azobis (isobutyronitrile) (AIBN, analytically pure) were purchased from Aladdin Chemistry. Commercial liquid electrolyte (1.0 M LiTFSI in DME:DOL=1:1 Vol% with 1.0% LiNO<sub>3</sub> additive) was purchased from dodo chem. Sublimed sulfur was purchased from Kermel Company. The lithium hexafluorophosphate (LiFePO<sub>4</sub>), N-methyl pyrrolidone (NMP), and Polyvinylidene fluoride (PVDF) were purchased from Sigma Aldrich. Acetylene black were purchased from Alfa Aesar. The commercial LiNi<sub>0.8</sub>Co<sub>0.1</sub>Mn<sub>0.1</sub>O<sub>2</sub> (NCM811) cathode (the areal mass loading of NCM811 is about 17.1 mg cm<sup>-2</sup>) were purchased from Wuhan Ruikome New Energy Company. All the chemicals were used as received without any further purification.

*Preparation of gel polymer electrolyte precursor:* Gel polymer electrolyte was prepared by in-situ polymerize method with polymer-monomer that contains in liquid electrolyte (LE). Typically, 1.5 wt% pentaerythritol tetraacrylate (PETEA) monomer was dissolved in a LE consisting of 1 M lithium bis(trifluoromethanesulfonyl)imide (LiTFSI) salt in a mixture of 1, 3-dioxolane (DOL)/dimethoxymethane (DME) (1:1 by volume) with 1 wt% LiNO<sub>3</sub>. After that, 1.5 wt% 2-Hydroxyethyl acrylate (HEA) as the cross-linker and 0.1 wt% 2, 2-azobis(2-methylpropionitrile) (AIBN) as the initiator were added into the mixture to obtain the transparent precursor solution. For polymerization, the precursor solution was thermally initiated at 70 °C for 30 min to form 3D cross-linked polymer electrolyte (termed as PHGPE). For comparison purpose, no hydroxyl modified polymer electrolyte was also prepared by polymerizing PETEA, and the fabrication procedure was similar to that of PHGPE except for the addition of HEA. The obtained sample was named as PGPE. All the procedures were operated in

an argon-filled glove box with the concentrations of moisture and oxygen below 0.1 ppm. For the fabrication of dry gels, the wet gels were first obtained by copolymerizing the monomers in the solvent of DME:DOL(1:1 Vol%), followed by rinsing with DME three times to remove impurities and un-reacted monomers. Finally, they were dried under vacuum at 60 °C to remove the solvent.

*Coin cell assembly and electrochemical characterizations:* The  $\text{LiFePO}_4$  (LFP) cathodes were prepared by casting a homogeneous slurry, which contains 80 wt.% LFP powder, 10 wt.% Acetylene black and 10 wt.% polyvinylidene fluoride (PVDF) with N-methyl-2-pyrrolidone (NMP) as the solvent, onto on a carbon-coated aluminum foil followed by a vacuum drying at 80 °C for 24 h. The sample electrodes were obtained by using a disk-cutter with a diameter of 10 mm. The areal mass loading of LFP cathode was about 3.0 mg  $\text{cm}^{-2}$ . Sulfur/carbon (S/C) composite was firstly prepared by heating the mixture of element sulfur and acetylene black at 155 °C for 12 h in Ar atmosphere. The sulfur electrodes were prepared by casting a homogeneous slurry that contains 70 wt% S/C composite powder, 20 wt% acetylene black and 10 wt% polyvinylidene fluoride (PVDF) with NMP as the solvent onto on carbon-coated aluminum foil followed by a vacuum drying at 50 °C for 24 h. The working electrodes were obtained by using a disk-cutter with a diameter of 10 mm. The areal mass loading of sulfur was about 1.5 mg  $\text{cm}^{-2}$ . All the cells were assembled in an Ar-filled glovebox and the electrochemical tests were carried out at ambient temperature. For symmetric cells assembling, two identical bare Li foils were used as the working electrode, Celgard 2400 polypropylene (PP) and the PHGPE were used as the separator and electrolyte, respectively. LMBs were assembled with LFP, commercial NCM811 and S cathodes, Celgard 2400 polypropylene (PP) separator and LM anodes. Accordingly, 120, 120 and 30  $\mu\text{L}$  of gel electrolyte precursor were added into the coin, respectively. After wetting, the assembled cells were placed into an electronic vacuum oven at 70 °C for 0.5 h to in-situ polymerize the precursor into gel polymer electrolyte. All the galvanostatic charge/discharge was performed on a Land CT2001A multichannel battery testing system. The cut-off voltage range of LFP full-cell was 2.5 – 4.0 V, the Li-S full cell

was 1.6 – 2.8 V, and the Li-NCM811 full-cell was 3.0 V – 4.2 V. The CV measurements of Li-S full-cell were carried out on an Autolab electrochemical working station with a voltage ranging from 1.5 V to 3.0 V at a scan rate of 0.2 mV s<sup>-1</sup>. Linear sweep voltammetry (LSV) was carried out from 0-5.5 V with a scanning rate of 1 mV s<sup>-1</sup>. The electrochemical impedance measurements were conducted by applying an AC voltage of 5 mV in the frequency range from 10<sup>-2</sup> Hz to 10<sup>5</sup> Hz. Lithium ion transference number ( $t_{Li^+}$ ) was calculated according to Bruce-Vincent-Evans method.<sup>36</sup> The ionic conductivity was measured with a configuration of stainless steel (SS)||electrolyte||SS in the temperature range of 20 - 70 °C. The ionic conductivity was calculated using the equation  $\sigma = L/(R_b \times A)$ , where  $R_b$  is the resistance from the EIS measurement,  $L$  represents the thickness of the electrolyte, and  $A$  is the area of the SS electrode.

*Numerical simulations:* The COMSOL simulation of Li deposition in different electrolytes was performed according to previously literatures.<sup>25</sup> The cell parameters in COMSOL simulation were set as follows. The diameter of Li nuclei was 200 nm. The gap between anode and cathode was set as 50  $\mu$ m. The overpotential of deposition was -200 mV vs. Li/Li<sup>+</sup> at the working electrode. The Li<sup>+</sup> diffusion coefficient was set to be  $1 \times 10^{-5}$  cm<sup>2</sup> s<sup>-1</sup>. The liquid electrolytes were confined in porous structures with different pore sizes: 1  $\mu$ m in the case of PP membrane, 50 nm in the case of PGPE electrolyte matrix, and 10 nm in the case of PHGPE electrolyte matrix. The surface charge was set as 10 eV on each material of the porous structures. The electrodeposition module was applied as the Einstein relation ( $D = \mu k_B T / q$ ).

*Characterizations:* The microstructure and morphology were investigated using a field-emission scanning electron microscope (SEM, Hitachi, S-4700) and transmission electron microscopy (TEM, Hitachi, HT7700 EXALENS). The Fourier transform infrared spectra were collected on a TENSOR27 spectrometer from Bruker. Thermogravimetric (TG) analysis was performed on a PerkinElmer analyzer (TA Instruments) in N<sub>2</sub> atmosphere at a heating ramp of 10 °C min<sup>-1</sup>. The X-ray photoelectron spectroscopy (XPS) depth profiles were carried out on an Ar<sup>+</sup> gas cluster ion beam (GCIB) equipped XPS analyzer from ThermoFischer (ESCALAB 250Xi spectrometer).

## Conflicts of interest

There are no conflicts to declare.

## Acknowledgement

This work is supported by the Natural Science Foundation of China (51802122), Opening Project of Key Laboratory of Optoelectronic Chemical Materials and Devices, Ministry of Education, Jiangnan University (JDGD-201811, JDGD-202007). The research of R. T, S. D and X-G. S was supported by the U.S. Department of Energy, Office of Science, Office of Basic Energy Sciences, Materials Sciences and Engineering Division under contract number DE-AC05-00OR22725.

## References

1. Y. Xiao, B. Han, Y. Zeng, S. S. Chi, X. Zeng, Z. Zheng, K. Xu and Y. Deng, *Adv. Energy Mater.*, 2020, **10**, 1903937.
2. S. Chen, R. Tao, J. Tu, P. Guo, G. Yang, W. Wang, J. Liang and S. Y. Lu, *Adv. Funct. Mater.*, 2021, **31**, 2101199.
3. S. Tang, Q. Lan, L. Xu, J. Liang, P. Lou, C. Liu, L. Mai, Y.-C. Cao and S. Cheng, *Nano Energy*, 2020, **71**, 104600.
4. Y. Liu, R. Tao, S. Chen, K. Wu, Z. Zhong, J. Tu, P. Guo, H. Liu, S. Tang, J. Liang and Y.-C. Cao, *J. Power Sources*, 2020, **477**, 228694.
5. J. B. Goodenough and K. S. Park, *J. Am. Chem. Soc.*, 2013, **135**, 1167–1176.
6. Y. G. Guo, J. S. Hu and L. J. Wan, *Adv. Mater.*, 2008, **20**, 2878–2887.
7. G. X. Huang, S. R. Chen, P. M. Guo, R. M. Tao, K. C. Jie, B. Liu, X. F. Zhang, J. Y. Liang and Y. C. Cao, *Chem. Engin. J.*, 2020, **395**.
8. G. X. Huang, P. M. Guo, J. Wang, S. R. Chen, J. Y. Liang, R. M. Tao, S. Tang, X. F. Zhang, S. J. Cheng, Y. C. Cao and S. Dai, *Chem. Engin. J.*, 2020, **384**.
9. G. X. Huang, P. Lou, G. H. Xu, X. F. Zhang, J. Y. Liang, H. H. Liu, C. Liu, S. Tang, Y. C. Cao and S. J. Cheng, *Journal of Alloys and Compounds*, 2020, **817**.
10. X. Q. Zhang, X. B. Cheng, X. Chen, C. Yan and Q. Zhang, *Adv. Funct. Mater.*, 2017, **27**.

11. Q. Zhao, Z. Tu, S. Wei, K. Zhang, S. Choudhury, X. Liu and L. A. Archer, *Angew. Chem. Int. Ed.*, 2018, **57**, 992–996.
12. Y. C. Li, S. Wan, G. M. Veith, R. R. Unocic, M. P. Paranthaman, S. Dai and X. G. Sun, *Adv. Energy Mater.*, 2017, **7**.
13. G. Y. Zheng, C. Wang, A. Pei, J. Lopez, F. F. Shi, Z. Chen, A. D. Sendek, H. W. Lee, Z. D. Lu, H. Schneider, M. M. Safont-Sempere, S. Chu, Z. N. Bao and Y. Cui, *Acs Energy Letters*, 2016, **1**, 1247–1255.
14. Y. Y. Liu, D. C. Lin, P. Y. Yuen, K. Liu, J. Xie, R. H. Dauskardt and Y. Cui, *Adv. Mater.*, 2017, **29**.
15. J. van den Broek, S. Afyon and J. L. M. Rupp, *Adv. Energy Mater.*, 2016, **6**, 1600736.
16. J. F. Wu, W. K. Pang, V. K. Peterson, L. Wei and X. Guo, *ACS Appl Mater Interfaces*, 2017, **9**, 12461–12468.
17. Z. Wang, R. Tan, H. Wang, L. Yang, J. Hu, H. Chen and F. Pan, *Adv Mater*, 2018, **30**.
18. M. Liu, D. Zhou, Y. B. He, Y. Z. Fu, X. Y. Qin, C. Miao, H. D. Du, B. H. Li, Q. H. Yang, Z. Q. Lin, T. S. Zhao and F. Y. Kang, *Nano Energy*, 2016, **22**, 278–289.
19. Y. Zhu, X. He and Y. Mo, *ACS Appl Mater Interfaces*, 2015, **7**, 23685–23693.
20. J. C. Bachman, S. Muy, A. Grimaud, H. H. Chang, N. Pour, S. F. Lux, O. Paschos, F. Maglia, S. Lupart, P. Lamp, L. Giordano and Y. Shao-Horn, *Chem. Rev.*, 2016, **116**, 140–162.
21. T. Famprikis, P. Canepa, J. A. Dawson, M. S. Islam and C. Masquelier, *Nat Mater*, 2019, **18**, 1278–1291.
22. L. Fan, S. Wei, S. Li, Q. Li and Y. Lu, *Adv. Energy Mater.*, 2018, **8**, 1702657.
23. J. Bae, Y. Qian, Y. Li, X. Zhou, J. B. Goodenough and G. Yu, *Energy Environ. Sci.*, 2019, **12**, 3319–3327.
24. J. Y. Song, Y. Y. Wang and C. C. Wan, *J. Power Sources*, 1999, **77**, 183–197.
25. P. Jaumaux, Q. Liu, D. Zhou, X. F. Xu, T. Y. Wang, Y. Z. Wang, F. Y. Kang, B. H. Li and G. X. Wang, *Angew. Chem. Int. Ed.*, 2020, **59**, 9134–9142.
26. T. H. Zhou, Y. Zhao, J. W. Choi and A. Coskun, *Angew. Chem. Int. Ed.*, 2021, **60**, 22791–22796.
27. X. G. Sun and J. B. Kerr, *Macromolecules*, 2006, **39**, 362–372.
28. X. G. Sun, G. Liu, J. B. Xie, Y. B. Han and J. B. Kerr, *Solid State Ionics*, 2004, **175**, 713–716.
29. K. R. Deng, Q. G. Zeng, D. Wang, Z. Liu, Z. P. Qiu, Y. F. Zhang, M. Xiao and Y. Z. Meng, *J. Mater. Chem. A*, 2020, **8**, 1557–1577.
30. H. Zhang, C. M. Li, M. Piszcz, E. Coya, T. Rojo, L. M. Rodriguez-Martinez, M. Armand and Z. B. Zhou, *Chem. Soc. Rev.*, 2017, **46**, 797–815.

31. Y. G. Zhou, X. Zhang, Y. Ding, J. Bae, X. L. Guo, Y. Zhao and G. H. Yu, *Adv. Mater.*, 2020, **32**.
32. S. H. Wang, Y. X. Yin, T. T. Zuo, W. Dong, J. Y. Li, J. L. Shi, C. H. Zhang, N. W. Li, C. J. Li and Y. G. Guo, *Adv. Mater.*, 2017, **29**.
33. Y. Z. Li, Y. B. Li, Y. M. Sun, B. Butz, K. Yan, A. L. Koh, J. Zhao, A. Pei and Y. Cui, *Nano Lett.*, 2017, **17**, 5171–5178.
34. Y. R. Wang, Q. L. Ni, Z. H. Liu, J. D. Zou and X. S. Zhu, *J. Polym. Res.*, 2011, **18**, 2185–2193.
35. X. Yang, M. Jiang, X. Gao, D. Bao, Q. Sun, N. Holmes, H. Duan, S. Mukherjee, K. Adair, C. Zhao, J. Liang, W. Li, J. Li, Y. Liu, H. Huang, L. Zhang, S. Lu, Q. Lu, R. Li, C. V. Singh and X. Sun, *Energy Environ. Sci.*, 2020, **13**, 1318–1325.
36. J. Evans, C. A. Vincent and P. G. Bruce, *Polymer*, 1987, **28**, 2324–2328.
37. H. Huo, B. Wu, T. Zhang, X. Zheng, L. Ge, T. Xu, X. Guo and X. Sun, *Energy Stor. Mater.*, 2019, **18**, 59–67.
38. J. Xiao, Q. Y. Li, Y. J. Bi, M. Cai, B. Dunn, T. Glossmann, J. Liu, T. Osaka, R. Sugiura, B. B. Wu, J. H. Yang, J. G. Zhang and M. S. Whittingham, *Nat. Energy*, 2020, **5**, 561–568.
39. S. R. Chen, J. M. Zheng, L. Yu, X. D. Ren, M. H. Engelhard, C. J. Niu, H. Lee, W. Xu, J. Xiao, J. Liu and J. G. Zhang, *Joule*, 2018, **2**, 1548–1558.
40. Y. Zhang, T.-T. Zuo, J. Popovic, K. Lim, Y.-X. Yin, J. Maier and Y.-G. Guo, *Mater. Today*, 2020, **33**, 56–74.
41. J. Zheng, M. H. Engelhard, D. Mei, S. Jiao, B. J. Polzin, J.-G. Zhang and W. Xu, *Nat. Energy*, 2017, **2**.
42. S. Xia, J. Lopez, C. Liang, Z. Zhang, Z. Bao, Y. Cui and W. Liu, *Adv Sci (Weinh)*, 2019, **6**, 1802353.
43. C. Xu, B. Sun, T. Gustafsson, K. Edström, D. Brandell and M. Hahlin, *J. Mater. Chem. A*, 2014, **2**, 7256–7264.
44. X. Cao, X. Ren, L. Zou, M. H. Engelhard, W. Huang, H. Wang, B. E. Matthews, H. Lee, C. Niu, B. W. Arey, Y. Cui, C. Wang, J. Xiao, J. Liu, W. Xu and J.-G. Zhang, *Nat. Energy*, 2019, **4**, 796–805.
45. R. Guo, D. N. Wang, L. Zuin and B. M. Gallant, *Acs Energy Lett.*, 2021, **6**, 877–885.
46. R. Guo and B. M. Gallant, *Chem. Mater.*, 2020, **32**, 5525–5533.
47. A. Ramasubramanian, V. Yurkiv, T. Foroozan, M. Ragone, R. Shahbazian-Yassar and F. Mashayek, *ACS Applied Energy Materials*, 2020, **3**, 10560–10567.
48. S. J. Tan, W. P. Wang, Y. F. Tian, S. Xin and Y. G. Guo, *Adv. Funct. Mater.*, 2021, **31**.
49. C. Ding, X. Fu, H. Li, J. Yang, J. L. Lan, Y. Yu, W. H. Zhong and X. Yang, *Adv. Funct. Mater.*, 2019, **29**, 1904547.

50. P. Shi, X. Q. Zhang, X. Shen, R. Zhang, H. Liu and Q. Zhang, *Adv. Mater. Techn.*, 2019, **5**, 1900806.
51. X. G. Sun, X. Q. Wang, R. T. Mayes and S. Dai, *Chemsuschem*, 2012, **5**, 2079–2085.
52. G. Li, F. Lu, X. Dou, X. Wang, D. Luo, H. Sun, A. Yu and Z. Chen, *J Am Chem Soc*, 2020, **142**, 3583–3592.
53. H. Qu, J. Zhang, A. Du, B. Chen, J. Chai, N. Xue, L. Wang, L. Qiao, C. Wang, X. Zang, J. Yang, X. Wang and G. Cui, *Adv Sci (Weinh)*, 2018, **5**, 1700503.
54. G. M. Zhou, L. C. Yin, D. W. Wang, L. Li, S. F. Pei, I. R. Gentle, F. Li and H. M. Cheng, *Design*, 2017, 55–74.
55. M. Marzantowicz, J. R. Dygas and F. Krok, *Electrochim. Acta*, 2008, **53**, 7417–7425.
56. R. Hu, H. Qiu, H. Zhang, P. Wang, X. Du, J. Ma, T. Wu, C. Lu, X. Zhou and G. Cui, *Small*, 2020, **16**, e1907163.
57. X. G. Sun and C. A. Angell, *Electrochem. Commun.*, 2009, **11**, 1418–1421.



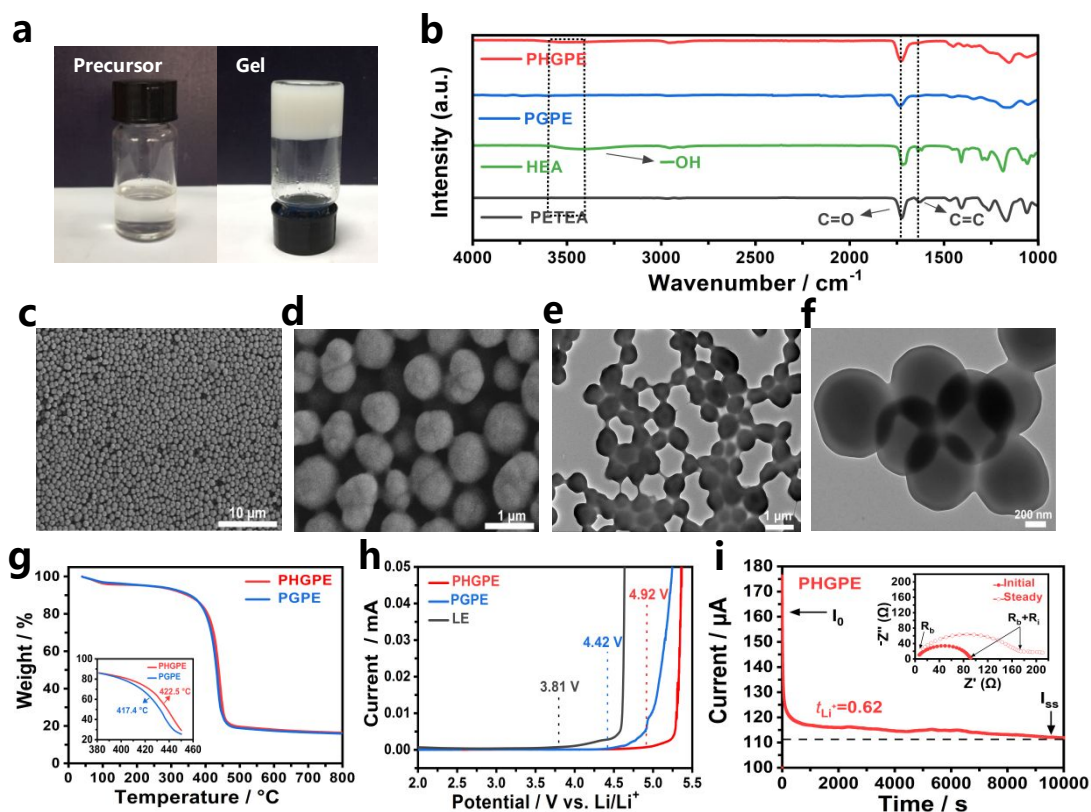


**Fig. 2** (a) The photographs of PHGPE before and after polymerization. (b) FTIR spectra of PHGPE, PGPE, HEA, PETEA. (c-d) SEM images of PHGPE polymer matrix. (e-f) TEM images of PHGPE polymer matrix. (g) TGA thermograms of the PHGPE matrix and PGPE matrix in  $\text{N}_2$  atmosphere. Inset is the local enlarged TGA curves. (h) LSV curves of PHGPE, PGPE and LE with stainless steel as the working electrode and Li foil as both counter and reference electrode at a scan rate of  $1 \text{ mV s}^{-1}$ . (i) The chronoamperometry profile of  $\text{Li}||\text{PHGPE}||\text{Li}$  battery at  $10 \text{ mV}$  polarization voltage. The inset shows the corresponding EISs of the symmetrical cell before and after polarization.

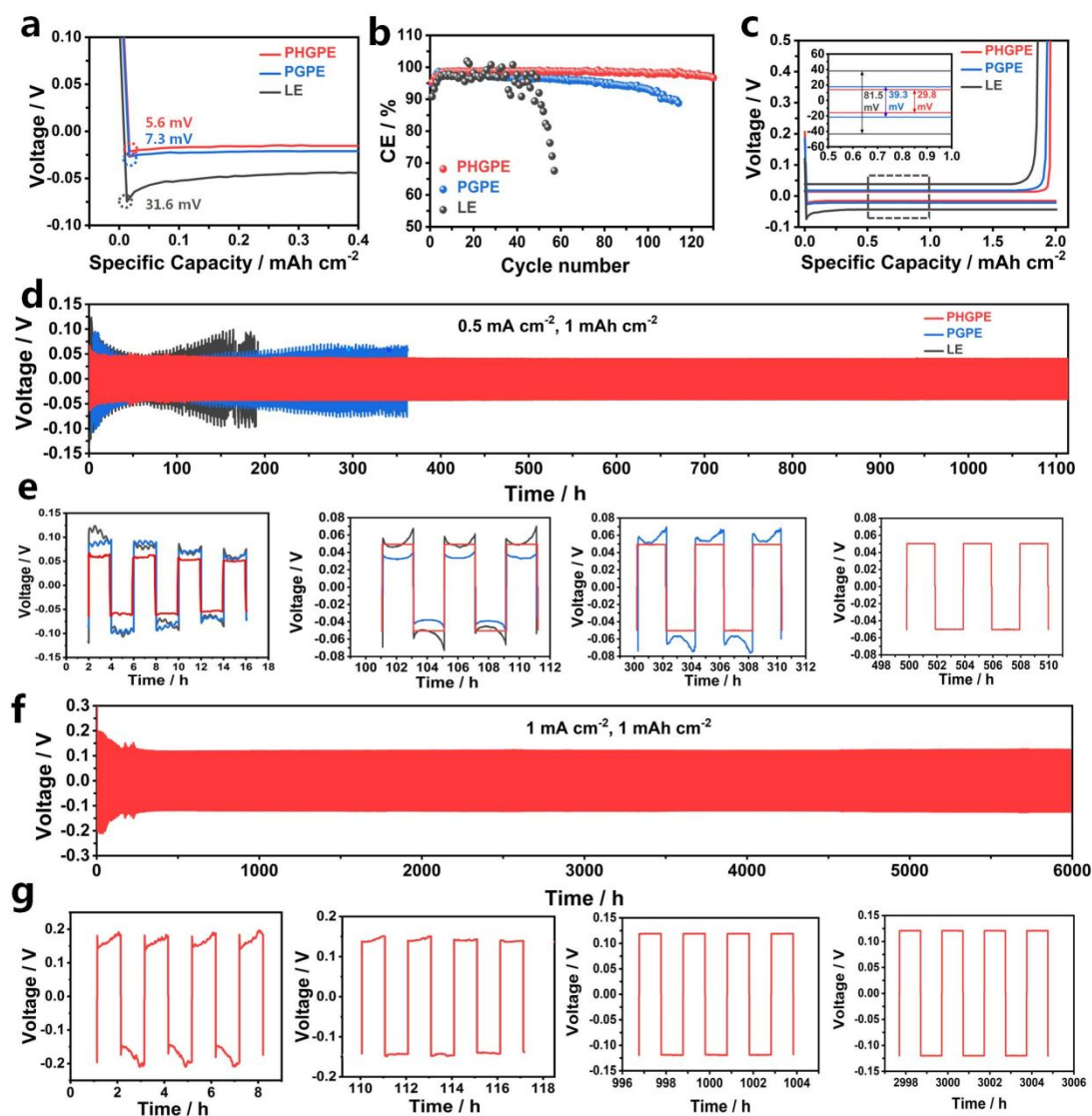


**Fig. 3** (a) Discharge profiles of Li||Cu half-cells with different electrolytes in the Li nucleation overpotential. (b) Coulombic efficiency of Li||Cu with different electrolytes at a current density of 0.5 mA cm<sup>-2</sup> with the capacity limited to 1 mAh cm<sup>-1</sup>. (c) Li stripping/plating curves of Li||Cu half-cells with different electrolytes at 0.5 mA cm<sup>-2</sup>. Insets are the enlarged images of the marked area. (d and e) Long-term polarization voltage profiles of Li||Li symmetric with different electrolytes at a current density of 0.5 mA cm<sup>-2</sup> with a capacity of 1 mAh cm<sup>-1</sup> and the selected polarization voltage profiles at different times. (f and g) Long-term polarization voltage profile of Li||PHGPE||Li symmetric cell at a current density of 1 mA cm<sup>-2</sup> with a capacity of 1 mAh cm<sup>-1</sup> and the corresponding selected polarization voltage profiles at different times.

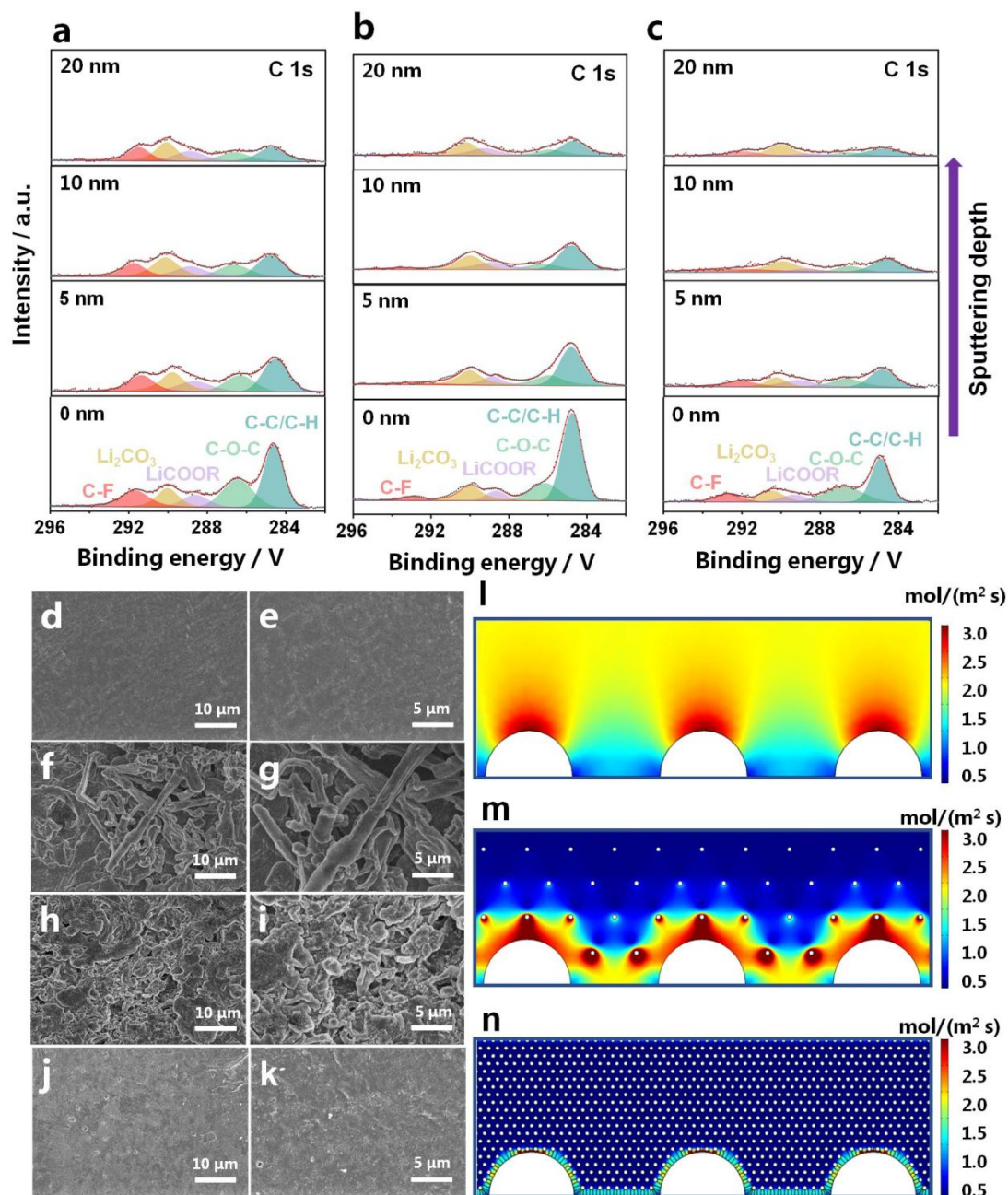


**Fig. 4** C1s HRXPS depth profiles of the SEI components on the LM anodes from Li||Li symmetric cells after 20 cycles in different electrolytes: (a) LE, (b) PGPE, (c) PHGPE. (d-e) SEM images of bare Li before cycling. SEM images of LM with different electrolytes in symmetric lithium batteries after 20 cycles with a cycling capacity of 1 mAh cm<sup>-2</sup> at 0.5 mA cm<sup>-2</sup>: (f-g) LE; (h-i) PGPE; (j-k) PHGPE. Numerical simulations of Li<sup>+</sup> flux distribution on the surface of LM anodes: (l) LE; (m) PGPE and (n) PHGPE system.

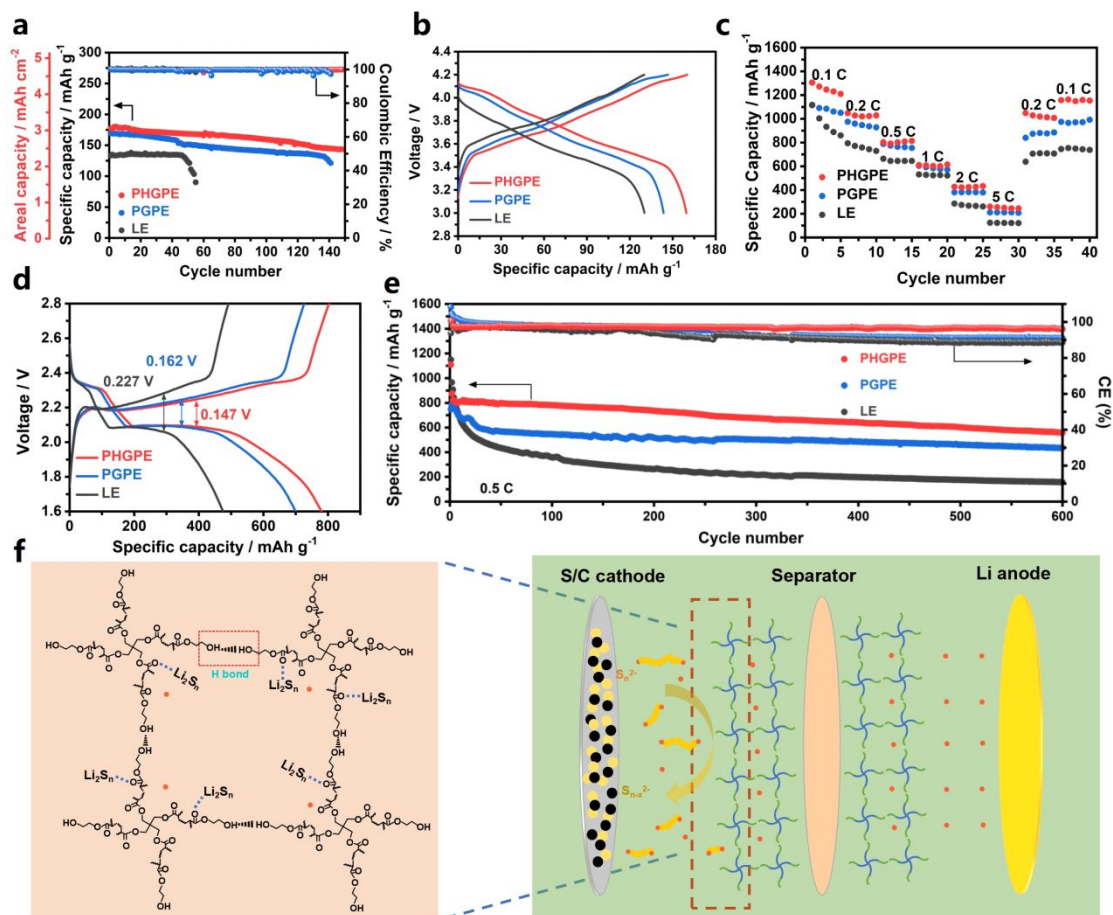


**Fig. 5** Electrochemical performances of Li||NCM811 full-cells in different electrolytes at 0.2 C: (a) Cycling performances; (b) Galvanostatic charge/discharge profiles for the 50<sup>th</sup> cycle. Electrochemical performances of Li-S full cells in different electrolytes: (c) Rate performances; (d) Galvanostatic charge/discharge profiles at 0.5 C; (e) Cycling performances at 0.5 C after two-cycle activations at 0.2 C. (f) Schematic illustration of the functional of the PHGPE in Li-S cell.

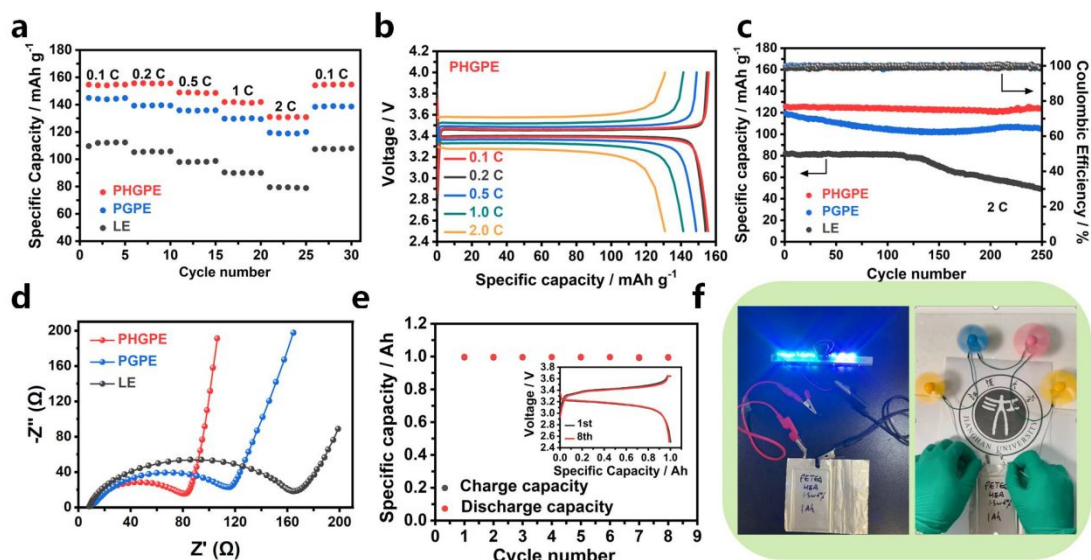


**Fig. 6** (a) Rate performances of Li||LFP in different electrolytes at various rates from 0.1 to 2 C. (b) Galvanostatic charge/discharge curves of Li||PHGPE||LFP at different rates. (c) Cycling performance of Li||LFP in different electrolytes at 2 C. (d) EIS Nyquist plots of Li||LFP batteries with different electrolytes after the 200<sup>th</sup> cycle. (e) Cycling performance of LFP||PHGPE||Li pouch cell. Inset is the galvanostatic charge/discharge profiles of the pouch cell at 1<sup>st</sup> and 8<sup>th</sup> cycles. (f) The practicality demonstration of Li||PHGPE||LFP pouch cell.